ACCEPTED FOR PUBLICATION IN APJ (9 MAR 2007)
Preprint typeset using LaTeX style emulateapj v. 10/09/06



# AN INFRARED STUDY OF THE LARGE-SCALE JET IN QUASAR PKS 1136−135

YASUNOBU UCHIYAMA,[1] C. MEGAN URRY,[2] PAOLO COPPI,[2] JEFFREY VAN DUYNE,[2] C. C. CHEUNG,[3,4] RITA M. SAMBRUNA,[5] TADAYUKI TAKAHASHI,[1,6] FABRIZIO TAVECCHIO,[7] AND LAURA MARASCHI[7]

*Accepted for publication in ApJ (9 Mar 2007)*

## ABSTRACT

We present *Spitzer* IRAC imaging of the large-scale jet in the quasar PKS 1136−135 at wavelengths of 3.6 and 5.8 $\mu$m, combined with previous *VLA*, *HST*, and *Chandra* observations. We clearly detect infrared emission from the jet, resulting in the most detailed multifrequency data among the jets in lobe-dominated quasars. The spectral energy distributions of the jet knots have significant variations along the jet, like the archetypal jet in 3C 273. The infrared measurements with IRAC are consistent with the previous idea that the jet has two spectral components, namely (1) the low-energy synchrotron spectrum extending from radio to infrared, and (2) the high-energy component responsible for the X-ray flux. The optical fluxes may be a mixture of the two components. We consider three radiation models for the high-energy component: inverse Compton scattering of cosmic microwave background (CMB) photons by radio-emitting electrons in a highly relativistic jet, synchrotron radiation by a second distinct electron population, and synchrotron radiation by ultra high energy protons. Each hypothesis leads to important insights into and constraints on particle acceleration in the jet, as well as the basic physical properties of the jet such as bulk velocity, transporting power, and particle contents.

*Subject headings:* galaxies: jets — infrared: galaxies — quasars: individual(PKS 1136−135) — radiation mechanisms: non-thermal

## 1. INTRODUCTION

Over the last decade, optical and X-ray observations made with the *Hubble Space Telescope* (e.g., Crane et al. 1993; Bahcall et al. 1995) and the *Chandra* X-ray Observatory (e.g., Chartas et al. 2000) have produced exquisite images of extragalactic kiloparsec-scale jets, completely changing our understanding of their properties. Currently, more than 70 (30) extragalactic jets and hotspots are known in the X-ray (optical) [8]; all but the few brightest jets were discovered by *Chandra* (*HST*).

The origin of the broad-band spectral energy distributions (SEDs) of large-scale quasar jets, constructed using *HST* and *Chandra* data, are the subject of active debate (for reviews, see Stawarz 2003; Harris & Krawczynski 2006). In luminous quasars with X-ray jets extending from the quasar nucleus out to hundreds of kiloparsec (e.g., Schwartz et al. 2000; Sambruna et al. 2004; Jorstad & Marscher 2004; Marshall et al. 2005; Siemiginowska et al. 2006), the X-ray intensity relative to the radio synchrotron flux is generally too high to be explained by a synchrotron-self-Compton model unless there is a huge deviation from equipartition (Chartas et al. 2000; Kataoka & Stawarz 2005). The radio, optical, and X-ray fluxes of a jet knot generally trace a peaked, inflected broad-band spectrum, which rules out the interpretation of X-rays as due to synchrotron radiation from a single population of electrons[9]. An alternative scenario, inverse-Compton (IC) scattering of CMB photons by high-energy electrons ($\gamma_e \sim 30$) in a highly relativistic jet with bulk Lorentz factor $\Gamma \sim 10$ (the beamed IC model: Tavecchio et al. 2000; Celotti, Ghisellini, & Chiaberge 2001) initially seemed a more natural way to explain the observed X-ray emission, but this process is also not free of problems (e.g., Atoyan & Dermer 2004). Finally, it is possible that the X-rays arise from synchrotron radiation from extremely energetic protons (Aharonian 2002). Determining which of these emission mechanisms produces the observed X-ray jets in powerful quasars is a strong motivation for more observations of radio-loud quasars, and has resulted in a rapid increase in the number of known X-ray and optical jets.

A new window to explore extragalactic large-scale jets has been opened by the *Spitzer Space Telescope*, which is capable of detecting jet infrared emission thanks to the excellent sensitivity of the Infrared Array Camera (IRAC; Fazio et al. 2004) and Multiband Imaging Photometer (MIPS; Rieke et al. 2004). The first example was the detection of infrared synchrotron radiation from jet knots in the quasar PKS 0637−752 with the *Spitzer* IRAC at wavelengths of 3.6 and 5.8 $\mu$m (Uchiyama et al. 2005). In terms of the beamed IC model, the infrared bandpass is particularly interesting since the bulk-Comptonization bump produced by cold electrons is expected to appear in the infrared (Georganopoulos et al. 2005). The absence of such features in the PKS 0637−752 jet rules out the jet model dynamically dominated by $e^+e^-$ pairs in the guise of the beamed IC model (Uchiyama et al. 2005). The MIPS observations of the jet in Centaurus A (Hardcastle et al. 2006; Brookes et al. 2006), and most recently, the results from IRAC and MIPS imaging photometry of the jet in M 87 (Shi et al. 2006) have been reported, which also demonstrate

[1] Department of High Energy Astrophysics, ISAS/JAXA, 3-1-1 Yoshinodai, Sagamihara, Kanagawa, 229-8510, Japan; uchiyama@astro.isas.jaxa.jp
[2] Yale Center for Astronomy and Astrophysics, Yale University, 260 Whitney Ave., New Haven, CT 06520-8121
[3] Jansky Postdoctoral Fellow; National Radio Astronomy Observatory
[4] Kavli Institute for Particle Astrophysics and Cosmology, Stanford University, Stanford, CA 94305
[5] NASA Goddard Space Flight Center, Code 661, Greenbelt, MD 20771
[6] Department of Physics, The University of Tokyo, 7-3-1 Hongo, Bunkyoku, Tokyo 113-0033, Japan
[7] Osservatorio Astronomico di Brera, via Brera 28, 20121 Milano, Italy
[8] An on-line list of extragalactic jets detected in the X-ray is found at `http://hea-www.harvard.edu/XJET/`, and that in the optical at `http://home.fnal.gov/~{}jester/optjets`

[9] It should be noted that, unlike the case of high-power jets, a synchrotron interpretation of X-ray emission has been well established for low-luminosity Fanaroff-Riley I jets (e.g., Hardcastle et al. 2001).

the power of *Spitzer* to study jet emissions in lower power jets (see also Perlman et al. 2007, for the M87 jet).

Now the three Great Observatories collectively offer the possibility to identify the radiation mechanisms operating in powerful quasar jets. In fact, when combined with the data from the *VLA*, *Hubble*, and *Chandra* (Jester et al. 2005, 2006), the *Spitzer* observation of the bright quasar 3C 273 shed new light on the riddle of X-ray jets (Uchiyama et al. 2006). The *Spitzer* IRAC photometry of the jet knots in 3C 273 indicated a two-component spectral energy distribution: a radio-to-infrared synchrotron component and a separate optical-to-X-ray component. The latter also seems likely to be of synchrotron origin, given the similar polarization of optical and radio light. The optical polarization, however, has not yet been measured with high precision, so this conclusion is not yet firm. Perhaps such a double synchrotron scenario is applicable to the radiation output from many quasar jets.

In this paper, we present *Spitzer* IRAC imaging of the powerful jet in the luminous quasar PKS 1136−135. Together with data from the *VLA*, *HST*, and *Chandra* (Sambruna et al. 2002, 2004, 2006a), our infrared photometry makes the SED of the PKS 1136−135 jet the most detailed and best constrained among *lobe-dominated* quasars. The jet in the quasar PKS 1136−135 is reminiscent of the 3C 273 jet (Sambruna et al. 2006a), demonstrating anti-correlation between radio and X-ray brightness, such that the radio intensity increases toward a hotspot while X-ray flux decreases. Applying the beamed IC model to the X-ray emission, this has recently been interpreted to imply *deceleration* of the jet (Sambruna et al. 2006a; Tavecchio et al. 2006). Here we analyze the multiwavelength jet emission in the light of the double synchrotron scenario recently outlined for the 3C 273 jet (Uchiyama et al. 2006). The redshift of PKS 1136−135 is $z = 0.554$, so we adopt a luminosity distance of $D_L = 3.20$ Gpc, for a concordance cosmology with $\Omega_{\rm m} = 0.27$, $\Omega_\Lambda = 0.73$, and $H_0 = 71$ km s$^{-1}$ Mpc$^{-1}$. The angular scale of $1''$ corresponds to 6.4 kpc.

## 2. OBSERVATIONS AND RESULTS

### 2.1. *Spitzer IRAC observations*

We observed PKS 1136−135 with *Spitzer* IRAC (Fazio et al. 2004) on 2005 June 10 as part of our Cycle-1 General Observer program (*Spitzer* program ID 3586). We used the pair of 3.6 and 5.8 $\mu$m arrays, observing the same sky simultaneously. The pixel size in both arrays is $\simeq 1\farcs22$. The point-spread functions (PSFs) are $1\farcs66$ and $1\farcs88$ (FWHM) for the 3.6 and 5.8 $\mu$m bands, respectively. The photometry with IRAC is calibrated to an accuracy of $\sim 3\%$ (Reach et al. 2005). We obtained a total of 50 frames per IRAC band, each with a 30-s frame time. The pipeline process (version S14.0.0) at the *Spitzer* Science Center yielded 50 calibrated images (Basic Calibrated Data). These well-dithered frames were combined into a mosaic image with a pixel size of $0\farcs2$ using MOPEX (Makovoz & Marleau 2005), which removes spurious sources such as cosmic rays and moving objects based on inter-frame comparisons. Finally, in order to align the IRAC image with respect to the VLA image, we set the center of the quasar in the IRAC image at the core position in the VLA image. In this way IRAC astrometry is estimated to be accurate to $\lesssim 0\farcs2$.

The infrared fluxes from the quasar core of PKS 1136−135 were measured as 2.2 and 4.0 mJy in the 3.6 and 5.8 $\mu$m bands, respectively (Table 1). These values do not reach the saturation limits of the IRAC arrays. Assuming that the infrared spectrum has a power law with $\alpha = 1$, as consistent with the ratio of the 3.6 and 5.8 $\mu$m fluxes, the luminosity in the 3–10 $\mu$m band amounts to $L_{3-10\mu{\rm m}} \simeq 2.6 \times 10^{45}$ ergs s$^{-1}$. In the model of Sambruna et al. (2006b), the infrared emission is assumed to arise from the inner jet, while the optical/UV emission originates in the accretion disk. Our infrared measurement is consistent with that model. If this is the case, the infrared fluxes determine the apparent luminosity of the synchrotron component.

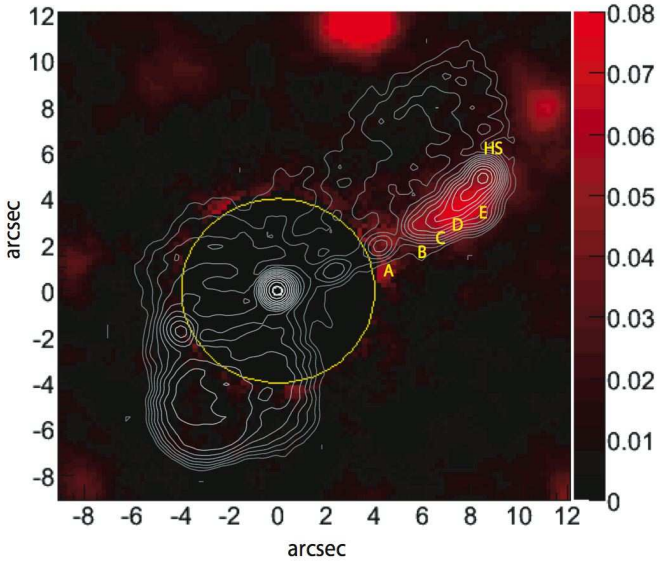


FIG. 1.— IRAC image of the PKS 1136−135 jet at 3.6 $\mu$m in units of MJy sr$^{-1}$ with core subtraction. North is up and east is to the left. The origin of the coordinate is set at the quasar core. A circular region with a radius of $4''$ around the core is blanked out, where the core subtraction is incomplete. An angular scale $1''$ corresponds to 6.4 kpc projected size. Superimposed on the IRAC image are radio contours on a logarithmic scale from the VLA 8.5 GHz map.

Inspection of the 3.6$\mu$m IRAC images clearly reveals the presence of an infrared jet that traces the extended radio jet. The IRAC 5.8 $\mu$m image also shows the jet emission, although its quality is worse than the 3.6 $\mu$m image. The extended PSF of the bright quasar core is significant at the location of the jet, amounting to $\sim$ 10–30% of the jet flux. In order to separate the jet infrared emission from the contaminating PSF wings of the core, we subtracted the PSF wings by making use of the PSF templates in a way similar to Uchiyama et al. (2005). Figure 1 shows the IRAC image of PKS 1136−135 in the 3.6 $\mu$m band after subtraction of the PSF wings of the quasar core. Infrared counterparts of the jet knots are clearly visible in the IRAC image, located $\sim 8''$–$12''$ from the core (knot B through hotspot HS). A possible counterpart of knot A is marginally found in the IRAC image, but it may be due to our incomplete PSF subtraction, so we regard the knot A flux only as an upper limit. The hotspot at the counter-jet side also suffers from the uncertainties of PSF subtraction; we do not find an infrared counterpart and place an upper limit of $f_{3.6} = 4$ $\mu$Jy at 3.6$\mu$m. Also, we do not detect extended infrared emissions from the radio lobes.

To construct the broad-band SEDs of jet knots using multifrequency data, we derived infrared flux densities of some knot features at 3.6 and 5.8 $\mu$m. Given the small separation of adjacent knots, typically $\sim 1''$, we utilized a PSF-fitting method (Uchiyama et al. 2006). Specifically, the jet image was fitted with a series of IRAC PSFs, fixing the PSF centers at the knot positions in the VLA 22 GHz radio image.

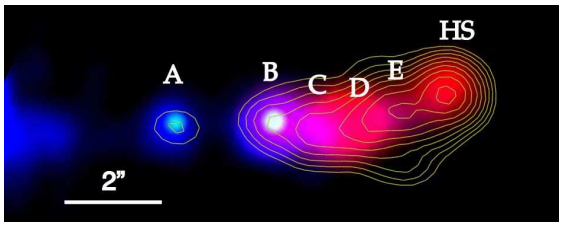


FIG. 2.— Composite image of the jet in PKS 1136−135 based on the data from *Spitzer* (shown as *red*), *HST* (*green dots* on knots A and B), and *Chandra* (*blue*). The superposed contours are from the *VLA* (8.5 GHz), highlighting the jet radio-emission (see also Fig. 1). Letters label the main features along the jet; knot A closest to the quasar. The multiwavelength image qualitatively illustrates the relative importance of low-energy component (radio–infrared) in the outer knots and high-energy one (optical–X-ray) in the inner knots.

However, this procedure did not fully determine knot by knot fluxes due mainly to a multiplicity of knots from C to E. We then fixed the flux density of knot E at $f_{3.6} = 2$ $\mu$Jy and $f_{5.8} = 4$ $\mu$Jy. We derived the systematic errors due to this treatment by changing the knot E flux in a range of $f_{3.6} = 0$–$3$ $\mu$Jy and $f_{5.8} = 0$–$6$ $\mu$Jy. The systematic errors are then added in quadrature to statistical ones. The photometric results determined in this way are listed in Table 1, where a combined flux is reported for knots C, D, and E (referred as knots CDE).

### 2.2. *Multifrequency Image*

In Figure 2 we present a three-color multifrequency image based on *Spitzer* infrared (*red*), *HST* optical (*green*), and *Chandra* X-rays (*blue*). The VLA 8.5 GHz radio contours in a logarithmic scale are overlaid. The infrared photometry at 3.6 $\mu$m is illustrated as a series of best-fitted PSFs of every knot after artificially shrinking the widths of the PSFs (1″ FWHM) to restore a resolution similar to the X-rays. At the positions of optically bright knots A and B we plot a *green* dot of $\sigma \simeq 0.''2$ to illustrate clear detections with the *HST* STIS and ACS (Sambruna et al. 2004, 2006a). The *Chandra* X-ray image in 0.3–8 keV band is smoothed with a Gaussian kernel of $0.''4$.

The jet morphology, or brightness pattern along the jet, in the infrared appears to be different from emission at shorter wavelengths. It is interesting to note that optically-bright features (knots A and B) are not particularly prominent in the infrared, while an infrared-bright knot D does not emit correspondingly strong optical light. The difference in the brightness pattern between the infrared and optical suggests a dramatic change of the spectral shape in the infrared-to-optical band along the jet. This emphasizes the importance of measuring infrared fluxes, together with the optical fluxes, in quasar jets.

Putting hotspot HS aside, the jet knots can be divided up into two parts: the *inner knots* (A and B) and the *outer knots* (C, D, and E). The inner knots are bright in both the optical and X-rays, and as such they are "high-energy dominated." Indeed the inner knots are most luminous in the X-rays, while the outer knots seem to have a luminosity peak in the far-infrared. To clarify this, we present the SEDs of the jet knots in the following section.

### 2.3. *Spectral Energy Distributions: Two-Component Nature*

We construct the broad-band SEDs of the jet knots using the new *Spitzer* IRAC data added to the *VLA*, *HST*, and *Chandra* data already presented in Sambruna et al. (2006a). Once again, the *Spitzer* IRAC provides crucial photometric points in characterizing the emissions of quasar jets (Uchiyama et al. 2005, 2006).

Table 1 summarizes the flux densities obtained with *VLA*, *Spitzer*, *HST*, and *Chandra*. The radio fluxes measured with the VLA at frequencies of 4.9, 8.46, and 22.5 GHz are taken from Sambruna et al. (2006a). Infrared photometry with the *Spitzer* IRAC is described in §2.1. In the optical, we list the flux densities from the *HST* ACS in two filters (Sambruna et al. 2006a): F475W (0.48 $\mu$m) and F814W (0.81 $\mu$m). We employed a somewhat different method for X-ray photometry compared with Sambruna et al. (2006a). Specifically, we here define two energy bands for photometry: 1–2 keV and 3–6 keV. Integrating over the entire jet (from knot A to hotspot HS) we found 203 and 57 counts in the 1–2 and 3–6 bands, respectively (also, 147 counts in the 0.6–1 keV band). The nominal energy $\varepsilon_{\rm norm}$ for each band is the mean energy weighted by the effective area: $\varepsilon_{\rm norm} = 1.56$ keV and 4.35 keV.

We reanalyzed the *Chandra* data sets that are fully described in Sambruna et al. (2006a), and constructed flux images (in units of photons cm$^{-2}$ s$^{-1}$ pix$^{-1}$) in the two bands, to which aperture photometry was applied. The object apertures for knots A/B and hotspot are a circle with a radius of $\simeq 0.''7$ centered on each feature, while that for knots CDE is a box enclosing knots C, D, and E. To correct for the interstellar absorption of $N_{\rm H} = 3.5 \times 10^{20}$ cm$^{-2}$, we multiplied the measured fluxes by a factor of 1.04 for the 1–2 keV band. The fudge factor slightly depends on the source spectrum such that it ranges from 1.040 to 1.048 for a power law with photon index $\Gamma = 1$–$3$. The photometry-based spectra are found to be consistent with the usual spectral analysis presented by Sambruna et al. (2006a). The photometric method is convenient when combining lower frequency data.

Care should be taken in interpreting the X-ray fluxes. First, the X-ray emission downstream of knot B does not show well discernible knots, and therefore the X-ray flux of knots CDE may not be related directly to the lower frequency fluxes. Second, in knot A there is an offset of $\sim 0.''4$ between the soft and hard X-ray peaks (Sambruna et al. 2006a). The X-ray spectrum derived for knot A may be contaminated by some unrelated emission, which makes the spectral shape inconsistent with a power law.

In Fig. 3, we present the SEDs from radio to X-rays for knots A, B, CDE, and hotspot HS. We note that the infrared fluxes we have measured with the *Spitzer* IRAC fill central points in the radio-to-X-ray SEDs of the jet knots, setting an important constraint on models of the broad-band emission. The *inner knots* (A and B) radiate most strongly in the X-ray. Also, significant (and probably flatter) optical emission is observed exclusively from the *inner knots*. The possible difference in slopes of the optical continuum between the *inner* and *outer knots* (Sambruna et al. 2006a) suggest different origins; the optical emission in the *inner knots* may belong to the same spectral component responsible for the X-ray emission (as suggested by Sambruna et al. 2006a, for knot A), while in the outer knots the optical emission is related to the radio synchrotron component.

These spectral characteristics are analogous to those of the jet in 3C 273 (Uchiyama et al. 2006), for which we identified two spectral components: (1) the low-energy synchrotron spectrum extending from radio to infrared, and (2) the high-energy component arising in the optical and smoothly connecting to the X-ray flux. We argued that the second component is likely to be of synchrotron origin as well, thus forming double-synchrotron spectra, because of the similarity of

TABLE 1
FLUX DENSITIES OF THE PKS 1136−135 CORE AND ITS JET KNOTS

| Region | Flux Density, $f_\nu$ | | | | | | | | |
|---|---|---|---|---|---|---|---|---|---|
| | $f_{5\ \mathrm{GHz}}$ (mJy) | $f_{8.5\ \mathrm{GHz}}$ (mJy) | $f_{22\ \mathrm{GHz}}$ (mJy) | $f_{5.8\ \mu\mathrm{m}}$ ($\mu$Jy) | $f_{3.6\ \mu\mathrm{m}}$ ($\mu$Jy) | $f_{0.81\ \mu\mathrm{m}}$ ($\mu$Jy) | $f_{0.48\ \mu\mathrm{m}}$ ($\mu$Jy) | $f_{1.56\ \mathrm{keV}}$ (nJy) | $f_{4.35\ \mathrm{keV}}$ (nJy) |
| Core | 463 | ··· | ··· | $4.0\times10^3$ | $2.2\times10^3$ | ··· | $1.5\times10^3$ | 170 | ··· |
| A | ··· | $3.8\pm0.4$ | ··· | $<5$ | $<4$ | $0.23\pm0.07$ | $0.17\pm0.03$ | $0.77\pm0.22$ | $0.72\pm0.29$ |
| B | $11\pm1.6$ | $9.3\pm0.9$ | $3.2\pm0.6$ | $4.8\pm2.2$ | $3.8\pm1.9$ | $0.33\pm0.09$ | $0.22\pm0.03$ | $2.0\pm0.34$ | $0.72\pm0.24$ |
| CDE | $192\pm19$ | $116\pm12$ | $47.5\pm9.5$ | $20\pm4$ | $9.5\pm2.0$ | $<0.46$ | $<0.23$ | $1.2\pm0.26$ | $0.67\pm0.25$ |
| HS | $200\pm20$ | $119\pm12$ | $43.9\pm8.8$ | $7.4\pm2.7$ | $4.6\pm2.0$ | $0.24\pm0.05$ | $<0.08$ | $<0.16$ | ··· |

NOTE. — The radio and optical data (extinction-corrected) for jet knots are taken from Sambruna et al. (2006a). The errors of optical fluxes are translated into those at a 90% level. The infrared fluxes of the jet knots are determined through PSF-fitting and quoted errors are dominated by their systematic errors. The X-ray fluxes listed with statistical errors (at a 90% confident level) are corrected for Galactic absorption using $N_{\rm H} = 3.5\times10^{20}$ cm$^{-2}$. Except for the infrared, the data of the core fluxes are taken from Gambill et al. (2003) assuming $\alpha_{\rm opt} = 0.5$ and $\alpha_{\rm X} = 0.7$.

TABLE 2
PHENOMENOLOGICAL MODEL PARAMETERS OF PKS 1136−135 JET

| Parameter | knot A | knot B | knots CDE | hotspot HS |
|---|---|---|---|---|
| $\alpha_1$ | 0.65 | 0.65 | 0.85 | 1.0 |
| $\nu_1$ (Hz) | $<3\times10^{13}$ | $2\times10^{13}$ | $3\times10^{13}$ | $5\times10^{13}$ |
| $L_1$ (erg s$^{-1}$) | $<1.3\times10^{43}$ | $3.1\times10^{43}$ | $1.7\times10^{44}$ | $1.2\times10^{44}$ |
| $\alpha_2$ | 0.75 | 0.70 | 0.50 | ··· |
| $L_2$ (erg s$^{-1}$) | $5.0\times10^{43}$ | $8.0\times10^{43}$ | $7.3\times10^{43}$ | ··· |

NOTE. — Equation (1) is adopted to characterize the SEDs.

polarization between optical and radio emission (though the degrees of optical polarization are not established yet).

Given the similarity to 3C 273, we model the radio-to-X-ray SEDs phenomenologically by the following function, namely, a double power-law with an exponential cutoff:

$$f_\nu = \sum_{i=1}^{2} \kappa_i \nu^{-\alpha_i} \exp\left[-\left(\frac{\nu}{\nu_i}\right)^{1/2}\right]. \quad (1)$$

The first term ($i = 1$) of the right-hand-side accounts for the low-energy spectrum and the second term ($i = 2$) describes the high-energy part. As there are no firm indication of spectral steepening at X-rays, we set an arbitrary cutoff at $\nu_2 = 1\times10^{19}$ Hz for the second component. For the inverse-Compton model described later (§3.1; see Fig. 5), however, the high-energy cutoff is located far beyond the X-ray domain, reaching very high-energy gamma-rays.

Table 2 lists the spectral parameters that well describe the knot SEDs shown in Fig. 3. Instead of the normalization, $\kappa_i$, we present the total apparent luminosity (without taking account of relativistic beaming) defined as $L = 4\pi D_L^2 \int f_\nu d\nu$ for each component, where the low-energy boundary of the integral is set at $10^9$ Hz and $10^{13}$ Hz for the first and second component, respectively. Knot B, the most X-ray luminous one, has a luminosity of $L_2 \simeq 8\times10^{43}$ erg s$^{-1}$ for the high-energy component, which indeed exceeds the luminosity of the low-energy component.

The spectral index of the low-energy component is in the range of $\alpha_1 \simeq 0.65$–$1.0$, which is determined by the radio spectra, as listed in Table 2. The cutoff frequency of the low-energy component, as constrained by the IRAC fluxes, is $\nu_1 = (2$–$5)\times10^{13}$ Hz in the cases of knots B, CDE, and hotspot HS; $\nu_1 < 3\times10^{13}$ Hz for knot A. The second spectral index is found to be $\alpha_2 \simeq 0.5$–$0.75$.

## 3. INTERPRETING THE HIGH-ENERGY COMPONENT

While the low-energy emission from quasar jets is undoubtedly of synchrotron origin, the production mechanism(s) of strong X-rays remains a matter of debate (e.g., Harris & Krawczynski 2006). Three radiation models have been proposed to explain the high-energy component: inverse-Compton scattering by radio-emitting electrons, synchrotron radiation by a second electron population, and synchrotron radiation by energetic protons[10]. In this section we consider each of these in turn.

There are reasons to think that jets are relativistic on large scales (Garrington et al. 1988) and thus beaming may be important. The Doppler beaming factor is defined as $\delta \equiv [\Gamma(1-\beta\cos\theta)]^{-1}$ where $\beta c$ is the velocity of the jet, $\Gamma = (1-\beta^2)^{-1/2}$ is the bulk Lorentz factor of the jet, and $\theta$ is the observing angle with respect to the jet direction. A one-sided jet with two-sided hotspots in this source is a sign of substantial relativistic beaming. The Doppler factor is, however, not well constrained for this jet. Throughout this section, all physical quantities are referred to a jet co-moving frame unless otherwise specified. The exceptions to this are the direction and velocity of the jet itself. It is assumed that a relativistically moving blob (as noted by knot or hotspot) has spherical geometry with a radius of $r = 1$ kpc (in the jet frame of reference)[11] occupied homogeneously with relativistic particles and magnetic fields ("one-zone" model with a filling factor of unity).

Before we discuss the high-energy emission component of the *jet knots* (like knot B), we derive a lower limit on the magnetic field strength in hotspot HS, based on the *absence* of the high-energy emission. We do not introduce beaming effects for hotspot HS ($\Gamma = \delta = 1$). Synchrotron photons are Compton upscattered by synchrotron-emitting electrons themselves, namely "synchrotron self-Compton" (SSC), which is known to be a primary component for the high-energy emission in bright hotspots such as those in Cygnus A (Harris, Carilli, & Perley 1994). In fact, since the average energy density of synchrotron photons (see Band & Grindlay 1985) in hotspot HS, $U_{\rm syn} \simeq 9L_{\rm syn}/(16\pi r^2 c) \simeq 100$ eV cm$^{-3}$, largely exceeds the CMB energy density of $U_{\rm CMB} = 0.26(1+z)^4$ eV cm$^{-3}$ $\simeq 1.5$ eV cm$^{-3}$, the SSC flux well exceeds the IC/CMB flux in the hotspot of PKS 1136−135. We found

[10] Yet another possibility includes the model of Dermer & Atoyan (2002), which invokes spectral hardening due to inverse-Compton cooling in the Klein-Nishina regime.

[11] The size of the emission region is not certain, as the knots are unresolved. The knot size is assumed to be similar to the 3C 273 jet.

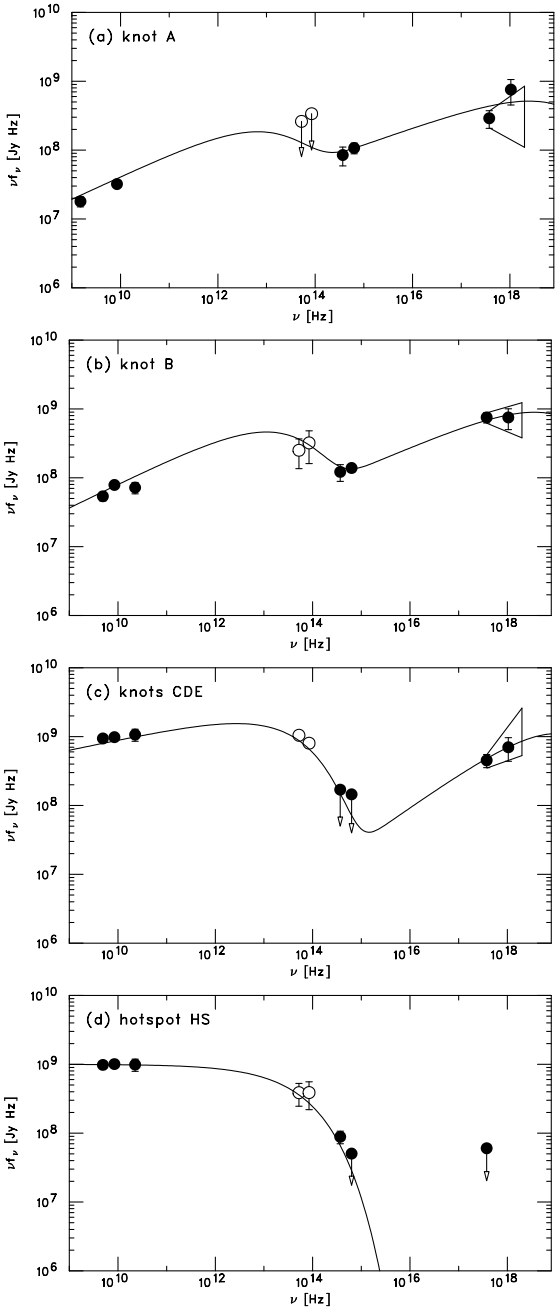


FIG. 3.— Broadband radio-to-X-ray SEDs for knots A, B, CDE, and hostspot HS in the powerful quasar 1136−135. IRAC 3.6 and 5.8 $\mu$m fluxes are shown as open circles. The data are summarized in Table 1. In addition, a flux density of $12.1 \pm 1.8$ mJy at 1.5 GHz (Sambruna et al. 2006a) is plotted in the SED of knot A. The two-component phenomenological model given as equation (1) is used to describe the data.

a lower limit on magnetic field as $B > 0.2$ mG in order not to violate the X-ray upper limit by the SSC emission. With an equipartition magnetic filed of $B_{\rm eq} = 0.66$ mG where the energy density of relativistic electrons is equal to that of magnetic fields, the one-zone SSC flux is an order of magnitude lower than the X-ray upper limit.

### 3.1. *Inverse-Compton Scattering by Ultra-Relativistic Jet*

We first discuss the second, X-ray-dominated component of the SED seen in the jet knots (knot B, in particular) in the framework of the beamed inverse-Compton model (Tavecchio et al. 2000; Celotti, Ghisellini, & Chiaberge 2001), which has been advocated in the previous papers for this jet (Sambruna et al. 2006a; Tavecchio et al. 2006). In this model, it is assumed that the jet has a highly relativistic bulk velocity, with a Lorentz factor $\Gamma \sim 10$ out to distances of hundreds of kiloparsecs, so that the CMB field *seen* by electrons is enhanced by a factor of $\Gamma^2$ in the jet comoving frame. The amplified CMB can be Compton up-scattered by high-energy electrons of $\gamma_e \sim 30$ into the observed X-rays. This model automatically requires that the jet direction is close to the line-of-sight, $\theta \sim \Gamma^{-1}$. (Such a condition, and therefore the beamed IC model itself, would not be favorable for a lobe-dominated quasar like PKS 1136−135. Later in this section, we shall briefly discuss this issue.)

It is interesting to test the beamed IC/CMB hypothesis, particularly for the PKS 1136−135 jet. The jet exhibits the evolution of multiwavelength emission along the jet, namely the increase of radio brightness accompanied by the decrease of X-ray brightness towards downstream. As detailed in Georganopoulos & Kazanas (2004), such a behavior can be interpreted, within the framework of the beamed IC radiation, as being due to deceleration of the jet (Sambruna et al. 2006a; Tavecchio et al. 2006). Specifically, Tavecchio et al. (2006) concluded that the bulk Lorentz factor of the jet decreases from $\Gamma \simeq 7$ (knot B) to $\Gamma \simeq 2$ (knot E). If the beamed IC scenario is confirmed, we gain a new probe of the flow structure of the large-scale jets.

Let us apply a synchrotron plus beamed IC/CMB model of Tavecchio et al. (2000) to the broadband SED of knot B. We also include SSC calculation for completeness. The both models adopt "one-zone" emission, assuming an emitting blob with homogeneously filled with relativistic particles and magnetic fields. It is interesting to note that in the case of no-beaming ($\Gamma = \delta = 1$), again, the average energy density of synchrotron photons in the knot, $U_{\rm syn} \simeq 12$ eV cm$^{-3}$, exceeds the CMB energy density. The energy distribution of radiating electrons is assumed to be of the form $N(\gamma) = k\gamma^{-s}$, having a low-energy cutoff at $\gamma_{\rm min} = 20$ and a high-energy exponential cutoff at $\gamma_{\rm max}$, where $\gamma$ denotes the electron's Lorentz factor. The number index of electrons is set to be $s = 2\alpha + 1 = 2.4$ based on a typical radio index in this jet ($\alpha \sim 0.7$), and the high-energy cutoff is determined to be $\gamma_{\rm max} = 4 \times 10^5$ to produce the infrared flux. The magnetic field strength is adopted as $B = B_{{\rm eq},\delta=1}\delta^{-1}$, where $B_{{\rm eq},\delta=1} = 175\,\mu$G; this relation ensures equipartition between relativistic electrons and magnetic fields, and keeps the peak frequency of the synchrotron radiation, $\nu_{\rm max} \propto \delta B \gamma_{\rm max}^2$. The bulk Lorentz factor itself does not explicitly affect the discussion made here and it is adopted to be $\Gamma = 15$.

Figure 4 shows the IC/CMB and SSC X-ray fluxes as a function of $\delta$, given the radio flux observed for knot B. Since the normalization of the electron distribution scales as $k \propto \delta^{-2}$ and the beaming pattern of the IC/CMB emission follows $\delta^{3+s}$ (Dermer 1995; Georganopoulos, Kirk, & Mastichiadis 2001), the IC/CMB flux scales as $k\delta^{3+s} \propto \delta^{1+s} = \delta^{3.4}$. The SSC flux scales as $k^2 B^{1+\alpha}\delta^{3+\alpha} \propto \delta^{-2}$, where $\alpha = (s-1)/2 = 0.7$. As such, if the jet is heavily beamed, $\delta \gg 1$, the IC/CMB flux is dominant. It reaches the observed X-ray flux at $\delta = 18.6$; the corresponding SED is shown in the top panel of Fig. 5. The SSC becomes a main component for $\delta < 1.4$. Even if we invoke a particle-dominated case of $U_e/U_B = 5000$, the SSC model requires a significant de-beaming of $\delta = 0.13$ to explain the observed X-rays, which is quite unlikely as the on-axis version of such jet emission becomes unacceptably luminous.

The radio-emitting electrons emit GeV $\gamma$-rays through the

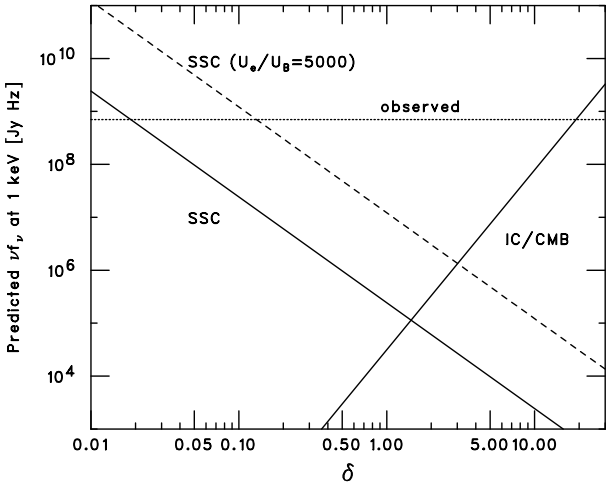


FIG. 4.— Predicted flux of IC/CMB and SSC at 1 keV as a function of the beaming factor ($\delta$) based on the observed radio flux of knot B. The observed X-ray flux is $7 \times 10^8$ Jy Hz (a horizontal *dotted* line). The IC/CMB emission is dominant for a large $\delta$, while SSC dominates the X-ray emission for de-beaming cases ($\delta < 1$). A dashed line shows the SSC prediction with the assumption of a significant deviation from equipartition ($U_e/U_B$ = 5000).

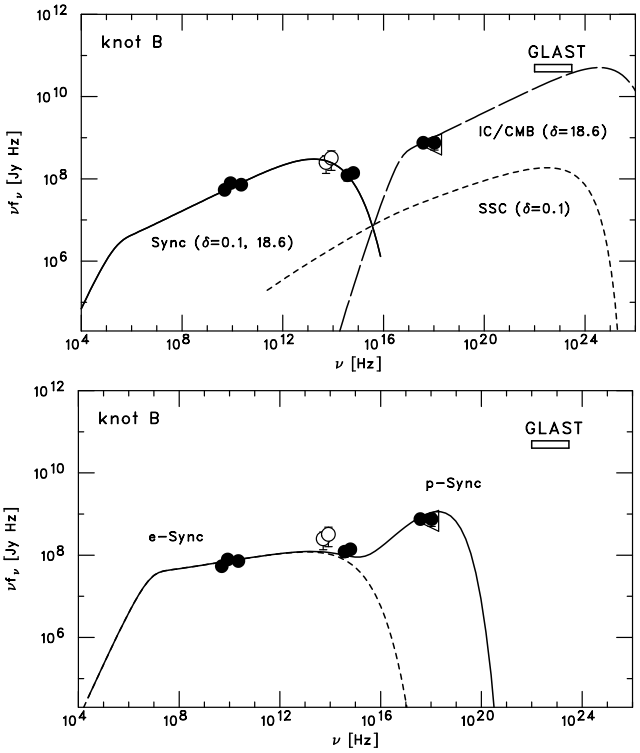


FIG. 5.— (*Top*) Synchrotron+IC/CMB modeling (*solid* and *dashed* curves) for knot B. The SED points are same as Fig. 3. A large beaming factor of $\delta$ = 18.6 is required to explain the X-ray flux. For illustrative purpose, it is also shown that if instead we invoke de-beaming ($\delta$ = 0.1: a *dotted* curve), the SSC luminosity becomes comparable to the synchrotron one. The expected sensitivity of the GLAST satellite (1 year $5\sigma$) is marked. (*Bottom*) Proton synchrotron model for the high-energy emission with moderate beaming $\Gamma = \delta = 3$ ($\theta \simeq 19°$). The low-energy emission is ascribed to electron synchrotron radiation. The *dotted* curve shows the electron component alone, while the *solid* line presents synchrotron radiation produced by both protons and electrons. Assuming equipartition between protons and magnetic fields, the magnetic field strength is $B_{\rm eq}$ = 1.7 mG. The production rate of electrons in terms of the energy content is about 5% of that of protons.

IC/CMB process (Fig. 5). The total radiative output is dominated by the multi-GeV $\gamma$-rays and their predicted flux just reaches the sensitivity offered by the upcoming GLAST satellite (see Georganopoulos et al. 2006, for the case of 3C 273). The quasar core is expected to show a similar level of $\gamma$-ray emission (Sambruna et al. 2006b); steadiness and hard spectrum are signatures of the large-scale emission. The observation of PKS 1136−135 (or quasar jets in general) with GLAST may be able to test the IC/CMB hypothesis. Note that the sub-TeV domains are subject to intergalactic absorption, which makes it difficult to investigate the jet emission with future ground-based Cherenkov telescopes.

The Doppler factor of $\delta \simeq 19$ required by the IC/CMB model implies an uncomfortably small angle between the jet and the line-of-sight, $\theta < 4°$. Tavecchio et al. (2006) also derived the maximum angle permitted as $\theta_{\rm max} = 3.°8$ for this jet. The small angle would make the jet quite long, $> (77/\sin\theta_{\rm max})$ kpc = 1.1 Mpc, and the total source extent would be as large as the largest quasar. The core-to-lobe flux ratio at 5 GHz, $R$, is an indicator of jet orientation. In the case of 1136−135, the core-to-lobe ratio of $R$ = 0.29 is obtained (Sambruna et al. 2004), thus designated as a *lobe-dominated* quasar. According to Laurent-Muehleisen et al. (1997), a sample of radio-loud quasars with a median value of $R$ = 0.52 have an average angle to the line-of-sight of $\langle\theta\rangle \sim 30°$ with simple beaming models. Also, the mean angle for steep-spectrum radio quasars is estimated as $\langle\theta\rangle \sim 30°$ (Urry & Padovani 1995). In this respect, a very small viewing angle $\theta < 4°$ for a lobe-dominated quasar like PKS 1136−135 is not favored in the light of simple unification schemes of radio-loud quasars and radio galaxies (Urry & Padovani 1995); a similar statement was made by Kataoka & Stawarz (2005). However, it should be kept in mind that *Chandra*-detected jets can be biased toward smaller jet angles, which alleviates a problem of the jet angle. We need a more direct means to distinguish currently proposed models (see §3.4).

### 3.2. *Synchrotron Radiation by Second Electron Population*

The large-scale jet in PKS 1136−135 is in many respects similar to the well-known jet of quasar 3C 273. As Sambruna et al. (2006a) have pointed out, in both jets, the radio emission brightens monotonically towards the terminal hotspot, while the upstream knots are brighter in X-rays. The two-component SEDs are also similar (cf, Uchiyama et al. 2006). In the case of 3C 273, since both the radio and optical emission are linearly polarized to a similar degree and in the same direction, it seems reasonable that the high-energy component, which contributes more than half the optical flux, should also arise from the synchrotron process (Uchiyama et al. 2006). Therefore we discuss the optical-to-X-ray component of 1136−135 in terms of synchrotron radiation produced by a second population of high-energy electrons. The suggestion of the presence of a second synchrotron component has been made in previous studies of other large-scale jets (e.g., Jorstad & Marscher 2004; Harris et al. 2004; Cheung et al. 2006).

Let the energy distribution of *accelerated* electrons be $Q(E_e)dE_e \propto E_e^{-s_2}dE_e$ for an energy interval of interest. The power-law slope of electrons is derived from the radiation slope as $s_2 = 2\alpha_2$ [see Eq. (1)] in a synchrotron-cooling regime as appropriate for optical and X-ray emission; the *cooled* electrons responsible for the observed radiation have a steeper number index of $s_2 + 1$ (see e.g., Kataoka et al. 2003). Then the spectral index of the high-energy component, $\alpha_2 \simeq 0.5$–$0.75$ corresponds to $s_2 \simeq 1.0$–$1.5$. However, within the framework of diffusive shock acceleration, the hardest possible electron distribution of acceleration would be

$Q(E_e) \propto E_e^{-1.5}$, in other words, $s_2 \geq 1.5$ (see Malkov & Drury 2001). The inferred index $s_2 \simeq 1.0$–$1.5$ would violate such a theoretical limit. This brings into question the idea that the second electron distribution is formed through the diffusive shock acceleration or that there is a second electron distribution at all. Note that the jet in 3C 273 has spectral index of $\alpha_2 \simeq 0.7$–$0.8$ corresponding to $s_2 \simeq 1.4$–$1.6$, which was considered to be compatible with the shock acceleration theory (Uchiyama et al. 2006).

The second synchrotron component in the PKS 1136−135 jet may instead be due to turbulent acceleration operating in the shear layers (Ostrowski 2000; Stawarz & Ostrowski 2002). The coexistence of two distinct types of acceleration, shock and turbulent acceleration, in the knots would naturally give rise to a double-synchrotron spectrum. More importantly, unlike the shock acceleration, a hard spectrum, $s_2 < 1.5$, can be expected to form in the case of turbulent acceleration (i.e., second-order Fermi acceleration). In fully turbulent shear layers, the time scale of turbulent acceleration can be estimated as $t_{\rm acc} \sim r_g c v_{\rm A}^{-2}$, where $r_g = E_e/(eB)$ is an electron gyroradius and $v_{\rm A}$ denotes the Alfvèn velocity. The turbulent acceleration has to compete against synchrotron losses, which is presumed to dominate over IC losses, with a timescale of

$$t_{\rm syn} = \frac{\gamma_e m_e c^2}{(4/3) c \sigma_{\rm T} U_B \gamma_e^2}, \tag{2}$$

where $\sigma_{\rm T}$ is the Thomson cross section, and $U_B = B^2/(8\pi)$ is the energy density of the magnetic field. By equating $t_{\rm acc} = t_{\rm syn}$—namely, balancing the acceleration and synchrotron loss rates—one obtains the maximum attainable energy limited by synchrotron losses:

$$E_{e,\rm max} \sim 6 \times 10^{15} \, \frac{v_{\rm A}}{c} \frac{1}{\sqrt{B_{-4}}} \, {\rm eV}, \tag{3}$$

where $B_{-4} = B/(10^{-4}{\rm G})$. To account for the observed X-rays with synchrotron radiation, one needs $E_{e,\rm max} \gtrsim 30 (B_{-4}\delta)^{-0.5}$ TeV (see Uchiyama et al. 2006), thus requiring $v_{\rm A} \gtrsim 5 \times 10^{-3} c$. This condition is reasonable with typical jet parameters.

### 3.3. *Proton Synchrotron Radiation*

Finally, we argue the possibility that the optical-to-X-ray emission may be due to synchrotron radiation by very high energy *protons* (Aharonian 2002). This model requires that protons in the jet are somehow accelerated to very high energies, $E_p \sim 10^{18}$ eV or more. Also, the magnetic field strength must be of the order $B \sim$ mG, so that energy equipartition between the relativistic *protons* and magnetic fields can be (roughly) realized. The knots and hotspots in the relativistic jets of powerful quasars and radio galaxies are indeed one of a few potential sites of cosmic-ray acceleration up to $E_p \sim 10^{20}$ eV (Hillas 1984). For example, the turbulent acceleration in the shear layer may be able to accelerate such ultra high energy protons (Ostrowski 2000).

The characteristic frequency and cooling time of proton synchrotron radiation can be written as

$$\nu_{\rm p-syn} \simeq 2.1 \times 10^{18} \left(\frac{B}{\rm mG}\right) \left(\frac{E_p}{10^{18}\,{\rm eV}}\right)^2 {\rm Hz}, \tag{4}$$

and

$$t_{\rm p-syn} \simeq 1.4 \times 10^{8} \left(\frac{B}{\rm mG}\right)^{-2} \left(\frac{E_p}{10^{18}\,{\rm eV}}\right)^{-1} {\rm yr}, \tag{5}$$

respectively (Aharonian 2002). (Note that the synchrotron cooling time is much shorter than the photo-meson cooling time at energies relevant here.) A total energy content of the magnetic field $B = 1$ mG integrated over a spherical knot with a radius of $r = 1$ kpc amounts to $W_B = 4.9 \times 10^{57}$ erg. If we assume equipartition between radiating protons and magnetic fields, $W_p = W_B$, the X-ray luminosity of synchrotron radiation by ultra-high-energy protons of $E_p \sim 10^{18}$ eV can be estimated roughly as

$$L_x \sim \frac{\eta W_p}{t_{\rm p-syn}} \sim \eta \frac{4.9 \times 10^{57}\,{\rm erg}}{1.4 \times 10^8\,{\rm yr}} \sim 1.1 \times 10^{42}\,\eta\,{\rm erg\,s^{-1}}, \tag{6}$$

where $\eta \sim 0.1$ denotes the fraction of kinetic energy of protons responsible for the X-ray emission. Relativistic beaming is not taken into account in this estimate. Roughly speaking, the luminosity scales with $B$ and $\delta$ such that $L_x \propto (B\delta)^4$. The expected luminosity agrees with typical (apparent) luminosity of the jet knots of quasars, $L_x \sim 10^{43}$ erg s$^{-1}$, if $B\delta \sim 6$ mG. Thus, very high energy protons rather than a second population of electrons, may explain the second synchrotron component extending from the optical to X-rays provided that both ultra-high-energy protons of $E_p \sim 10^{18}$ eV and a magnetic field of $B \sim$ mG are present in the jet knots. Under the proton-synchrotron hypothesis, the low-energy synchrotron emission may be accounted for by accompanying electrons.

To be specific, we modeled the high-energy spectral component of knot B with proton synchrotron radiation. We adopt mild beaming of $\delta = \Gamma = 3$ ($\theta \simeq 20°$). The low-energy spectral component was simultaneously modeled by electron synchrotron radiation with taking account of the effects of significant synchrotron cooling. It is assumed that during $\Delta t = 10^7$ years, protons and electrons are injected continuously into the emission volume ($r = 1$ kpc) with the distributions characterized by number index $s_p$ and $s_e$ and by the maximum energy $E_{p,\rm max}$ and $E_{e,\rm max}$: $\dot{Q}(E) = kE^{-s}\exp(-E/E_{\rm max})$. In the bottom panel of Fig. 5, we present the broadband SED reproduced by the proton synchrotron model with the equipartition magnetic field of $B = 1.7$ mG, the index of the power-law distribution of *accelerated* particles $s_p = s_e = 1.8$, and the maximum energy of $E_{p,\rm max} = 4.7 \times 10^{17}$ eV and $E_{e,\rm max} = 1 \times 10^{11}$ eV. The injection rate of electrons, in terms of energy content $\int \dot{Q}(E) dE$, is about 5% of that of protons. The injected electrons suffer from severe synchrotron cooling. Even radio-emitting electrons have a cooling time of only $\sim 10^4$ years, which requires *in-situ* acceleration of electrons. The infrared-emitting electrons have a lifetime of $\sim 10^2$ years, implying that each knot is a currently (within $10^2$ years) active site of particle acceleration.

The energy density of protons $U_p$, which is equal to $U_B$, can be calculated by $U_p \simeq (\Delta t/V) \int \dot{Q}_p(E) dE \simeq 7.4 \times 10^4$ eV cm$^{-3}$ with $V = 4\pi r^3/3$, since synchrotron cooling of protons is not effective. The kinetic power of the jet, estimated as $L_{\rm jet} \sim \pi r^2 \Gamma^2 \beta c (U_p + U_B)$, amounts to $L_{\rm jet} \sim 2 \times 10^{48}$ erg s$^{-1}$. This estimate is not sensitive to the choice of $\Gamma$ as long as the equipartition condition is fulfilled. A large power has to be carried by the protons and magnetic fields in the jet to produce the X-ray emission via a proton-synchrotron process. The black hole mass that powers the jet is estimated to be $4.6 \times 10^8 M_\odot$ (Oshlack et al. 2002) using the empirical relation to the width of the H$\beta$ line and the optical continuum luminosity. The black hole mass corresponds to the Eddington luminosity of $L_{\rm Edd} \simeq 6 \times 10^{46}$ erg s$^{-1}$. Therefore, the proton synchrotron model requires the jet to be *super-Eddington*,

$L_{\rm jet} \gg L_{\rm Edd}$. This issue would pose a problem for the proton synchrotron model, though it may be alleviated by assuming that the knots present the locations of *power peaks* due to modulated activity of the central engine.

### 3.4. *Possible Discriminator of the Radiation Models: Polarization of Optical Light*

We emphasize here that optical polarimetry can be an effective way of discriminating the radiation models responsible for the optical-to-X-ray emission of the jet in PKS 1136−135, and of quasar jets in general. In the beamed IC interpretation, if the optical fluxes belong to the IC component, the optical and X-ray emission are due to Compton up-scattering off the amplified CMB by high-energy electrons of $\gamma_e \sim 3$ (optical) and $\gamma_e \sim 100$ (X-ray). Unlike in the case of synchrotron models, the X-rays are expected to be *unpolarized* and the optical light is nearly unpolarized at most a few percent of polarization (Uchiyama & Coppi, in preparation)[12]. Precise polarization measurements in the optical can in principle verify (or discard) the beamed IC model. Unfortunately, there have been no useful polarization observations of quasar jets with *HST* so far. Only for 3C 273, early *HST* polarimetry of the jet was done but with the pre-COSTAR FOC and low significances (Thomson et al. 1993). As was recently performed for nearby radio galaxies by Perlman et al. (2006), new, deep polarimetry of quasar jets on large-scales is highly encouraged, although the optical emission from the jet knots is generally faint, say $< \mu$Jy (Sambruna et al. 2004).

## 4. SUMMARY

We have detected the infrared emission from the kiloparsec-scale jet in the quasar PKS 1136−135 with the *Spitzer Space Telescope*. Using the new *Spitzer* data together with deep *Chandra*, *Hubble*, and multi-frequency VLA observations from Sambruna et al. (2006a), we construct the broadband spectral energy distributions along the large-scale jet. The SEDs of the jet knots are comprised of two components: radio-to-infrared synchrotron emission and a separate high-energy component responsible for X-rays, which may extend down to the optical. In total, each component has a similar apparent luminosity of the order of $L_{\rm rad} \sim 10^{44}$ erg s$^{-1}$.

The origin of the high-energy component has significant implications to the properties of particle acceleration in a relativistic jet as well as jet dynamics. We consider three radiation models that have been proposed to explain the high-energy component: inverse-Compton scattering in a highly relativistic jet, synchrotron radiation by a second electron population, and synchrotron radiation by highly energetic protons.

In terms of the double synchrotron scenario, a flat spectrum of the second synchrotron component, $\alpha_2 \sim 0.5$, would turn down diffusive shock acceleration as the mechanism of electron acceleration to very high energies, $> 30$ TeV. Instead turbulent acceleration in the shear layers may explain the second population of electrons giving rise to the flat spectrum. In the beamed IC interpretation, a jet orientation with respect to the observer of $\theta < 4^\circ$ is required, which is not quite favorable given the small core-to-lobe ratio of this object. Future optical polarimetry or $\gamma$-ray observations with GLAST may be able to test the beamed IC model. The proton synchrotron model requires a relatively large magnetic field of $\sim 1.7$ mG, and consequently large kinetic power of $L_{\rm jet} \simeq 2 \times 10^{48}$ erg s$^{-1}$ $\sim 30 L_{\rm Edd}$, with efficient acceleration of protons to $E_{p,\rm max} \simeq 5 \times 10^{17}$ eV. If this is the case, one can probe particle acceleration at very high energies, higher than any other known objects in the Universe.

We thank the referee, Eric Perlman, for his careful reading of the manuscript and valuable suggestions. This work is based on observations made with the Spitzer Space Telescope, which is operated by the Jet Propulsion Laboratory, California Institute of Technology under NASA contract 1407. Support for this work was provided by NASA through Contract Number RSA 1265389 issued by JPL/Caltech. The National Radio Astronomy Observatory is operated by Associated Universities, Inc. under a cooperative agreement with the National Science Foundation.

[12] Compton up-scattering by a highly relativistic jet in which a population of cold electrons with $\gamma_e \simeq 1$ (in the jet frame) exists, namely "bulk Comptonization", can yield in principle a high degree of polarization for a jet angle $\theta \simeq \Gamma^{-1}$ (Begelman & Sikora 1987). For $\gamma_e$ of a few as relevant here, however, the polarization is largely suppressed.

## REFERENCES

Aharonian, F. A. 2002, MNRAS, 332, 215
Atoyan, A. M., & Dermer, C. D. 2004, ApJ, 613, 151
Bahcall, J. N., Kirhakos, S., Schneider, D. P., Davis, R. J., Muxlow, T. W. B., Garrington, S. T., Conway, R. G., & Unwin, S. C. 1995, ApJ, 452, L91
Band, D. L., & Grindlay, J. E. 1985, ApJ, 298, 128
Begelman, M. C., & Sikora, M. 1987, ApJ, 322, 650
Brookes, M. H., Lawrence, C. R., Keene, J., Stern, D., Gorijan, V., Werner, M., & Charmandaris, V. 2006, ApJ, 646, L41
Celotti, A., Ghisellini, G., & Chiaberge, M. 2001, MNRAS, 321, L1
Chartas, G., et al. 2000, ApJ, 542, 655
Cheung, C. C., Stawarz, Ł., & Siemiginowska, A. 2006, ApJ, 650, 679
Crane, P., et al. 1993, ApJ, 402, L37
Dermer, C. D. 1995, ApJ, 446, L63
Dermer, C. D., & Atoyan, A. M. 2002, ApJ, 568, L81
Fazio, G., et al. 2004, ApJS, 154, 10
Gambill, J. K., Sambruna, R. M., Chartas, G., Cheung, C. C., Maraschi, L., Tavecchio, F., Urry, C. M., & Pesce, J. E. 2003, A&A, 401, 505
Garrington, S. T., Leahy, J. P., Conway, R. G., & Laing, R. A. 1988, Nature, 331, 147
Georganopoulos, M., & Kazanas, D. 2004, ApJ, 604, L81
Georganopoulos, M., Kazanas, D., Perlman, E., & Stecker, F. W. 2005, ApJ, 625, 656
Georganopoulos, M., Kirk, J. G., & Mastichiadis, A. 2001, ApJ, 561, 111
Georganopoulos, M., Perlman, E., Kazanas, D., & McEnery J. 2006, ApJ, 653, 5
Hardcastle, M. J., Birkinshaw, M., & Worrall, D. M. 2001, MNRAS, 326, 1499
Hardcastle, M. J., Kraft, R. P., & Worrall, D. M. 2006, MNRAS, 368, L15
Harris, D. E., Carilli, C. L., Perley, R. A. 1994, Nature, 367, 713
Harris, D. E., & Krawczynski, H. 2006, ARA&A, 44, 463
Harris, D. E., Mossman, A. E., & Walker, R. C. 2004, ApJ, 615, 161
Hillas, A. M. 1984, ARA&A, 22, 425
Jester, S., Harris, D. E., Marshall, H. L., & Meisenheimer, K. 2006, ApJ, 648, 900
Jester, S., Röser, H.-J., Meisenheimer, K., & Perley, R. A. 2002, A&A, 385, L27
Jester, S., Röser, H.-J., Meisenheimer, K., & Perley, R. A. 2005, A&A, 431, 477
Jorstad, S. G., & Marscher, A. P. 2004, ApJ, 614, 615
Kataoka, J., Leahy, J. P., Edwards, P. G., Kino, M., Takahara, F., Serino, Y., Kawai, N., & Martel, A. R. 2003, A&A, 410, 833
Kataoka, J., & Stawarz, Ł. 2005, ApJ, 622, 797
Laurent-Muehleisen, S. A., Kollgaard, R. I., Ryan, P. J., Feigelson, E. D., Brinkmann, W., Siebert, J. 1997, A&AS, 122, 235
Makovoz, D., & Marleau, F. R. 2005, PASP, 117, 1113
Malkov, M. A., & Drury, L. O'C. 2001, Rep. Prog. Phys., 64, 429

Marshall, H. L., et al. 2005, ApJS, 156, 13
Oshlack, A. Y. K. N., Webster, R. L., & Whiting, M. T. 2002, ApJ, 576, 81
Ostrowski, M. 2000, MNRAS, 312, 579
Perlman, E. S., et al. 2006, ApJ, 651, 735
Perlman, E. S., et al. 2007, submitted to ApJ
Rieke, G. H., et al. 2004, ApJS, 154, 25
Reach, W. T., et al. 2005, PASP, 117, 978
Sambruna, R. M., Gambill, J. K., Maraschi, L., et al. 2004, ApJ, 608, 698
Sambruna, R. M., Gliozzi, M., Donato, D., Maraschi, L., Tavecchio, F., Cheung, C. C., Urry, C. M. Wardle, J. F. C. 2006a, ApJ, 641, 717
Sambruna, R. M., Gliozzi, M., Tavecchio, F., Maraschi, L., & Foschini, L. 2006b, ApJ, 652, 146
Sambruna, R. M., Maraschi, L., Tavecchio, F., et al. 2002, ApJ, 571, 206
Schwartz, D. A., et al. 2000, ApJ, 540, L69
Siemiginowska, A., Stawarz, Ł., Cheung, C. C., Harris, D. E., Sikora, M., Aldcroft, T. L., & Bechtold, J. 2006, ApJ, in press (astro-ph/0611406)
Shi, Y., Rieke, G. H., Hines, D. C., Gordon, K. D., Egami, E. 2006, ApJ, in press (astro-ph/0610494)
Stawarz, Ł. 2003, Chinese Journal of Astronomy and Astrophysics Supplement, 3, 383
Stawarz, Ł., & Ostrowski, M. 2002, ApJ, 578, 763
Tavecchio, F., Maraschi, L., Sambruna, R. M., Gliozzi, M., Cheung, C. C., Wardle, J. F. C., Urry, C. M. 2006, ApJ, 641, 732
Tavecchio, F., Maraschi, L., Sambruna, R. M., Urry, C. M. 2000, ApJ, 544, L23
Thomson, R. C., Mackay, C. D., & Wright, A. E. 1993, Nature, 365, 133
Uchiyama, Y., Urry, C. M., Van Duyne, J., Cheung, C. C., Sambruna, R. M., Takahashi, T., Tavecchio, F., & Maraschi, L. 2005, ApJ, 631, L113
Uchiyama, Y., Urry, C. M., Cheung, C. C., Jester, S., Van Duyne, J., Coppi, P., Sambruna, R. M., Takahashi, T., Tavecchio, F., & Maraschi, L. 2006, ApJ, 648, 910
Urry, C. M., & Padovani, P. 1995, PASP, 107, 803